Hydraulic fracturing: Laboratory evidence of the brittle-to-ductile transition with depth

Runhua Feng[1*], Shuo Liu[1] , Joel Sarout[2] , Jeremie Dautriat[2], Zhiqi Zhong[1,3], Reza Rezaee[1], Mohammad Sarmadivaleh[1*]

[1]School of WASM: Minerals, Energy and Chemical Engineering, Curtin University, 26 Dick Perry Ave, Kensington, WA 6151 Australia

[2]CSIRO Energy, Perth, WA 6151, Australia

[3] College of Energy, Chengdu University of Technology, Chengdu, China

*Corresponding author:

E-mail address: runhua.feng@student.curtin.edu.au (R.Feng);
mohammad.sarmadivaleh@curtin.edu.au (M.Sarmadivaleh)

Highlights:

- Hydraulic fracturing experiments are conducted on synthetic materials exhibiting a wide range of mechanical properties under true triaxial stresses with a low (σ_v = 6.5 MPa, σ_H =3 MPa, and σ_h =1.5MPa), and a higher (15 MPa, 10 MPa, and 5MPa) confinement where the wellbore pressure, three dimensional (3D) and volumetric strain induced by hydraulic fracturing are monitored and interpreted.
- The geometry of hydraulic fracture is highly inclined to the maximum horizontal σ_H (or vertical σ_v) stresses in brittle/semi-brittle samples; in contrast, the orientation angle is reduced in semi-ductile samples, and nearly reaches to zero (parallel to σ_H and σ_v) for ductile samples.
- The viscoelastic stress modelling explains the distinct characteristics of hydraulic fracturing induced deformation among the tested samples subjected to true triaxial stress state.
- The intermediate stress plays a profound role in hydraulic fracture (HF) propagation subjected to normal faulting regime, i.e., the transition of intermediate strain are temporally observed from brittle to ductile samples.
- The fracturing area are shown to be reduced as the decrease of brittleness for either low or higher confinement; the tortuosity and roughness of fracture surface increases as the confinement.

Abstract

Understanding the propagation of hydraulic fracture (HF) is essential for effectively stimulating the hydrocarbon production of unconventional reservoirs. Hydraulic fracturing may induce distinct failure modes within the formation, depending on the rheology of the solid and the *in-situ* stresses. A brittle-to-ductile transition of HF is thus anticipated with increasing depth, although only scarce data are available to support this hypothesis. Here we carry out laboratory hydraulic fracturing experiments in artificial geomaterials exhibiting a wide range of rheology: cubic samples 50x50x50 mm^3 in size are subjected to true triaxial stresses with either a low (σ_v = 6.5 MPa, σ_H =3 MPa, and σ_h =1.5MPa), or a higher (15 MPa, 10 MPa, and 5MPa) confinement. The 3D strains induced by hydraulic fracturing are monitored and interpreted; X-ray Computed Tomography (CT) imaging is used to document the HF geometry; and viscoelastic modelling of the tested materials is also conducted to explain the distinct geometry of hydraulic fracture subjected to the stress state. Finally, a correlation between the normalized fracture area (A_{FN}) and the brittleness index (BI) of tested samples is introduced. Our results reveal that: (i)The intermediate stress plays a profound role in hydraulic fracture propagation subjected to the normal faulting regimes (i.e., the transitional intermediate strain observed from brittle to ductile samples); (ii) The orientation angle of hydraulic fracture is highly inclined to the maximum horizontal σ_H (or vertical σ_v) stresses in brittle/semi-brittle samples; as BI decreases, the angle inclination is reduced for that of semi-ductile samples, finally reaches to zero (parallel to σ_H and σ_v) in ductile sample. (iii) The normalized fracturing area (A_{FN}) decreases as the decrease of BI among different samples under either low or higher confinement. The results of viscoelastic modelling explain the distinct characteristics of hydraulic fracturing induced deformation among the tested samples subjected to true triaxial stress state. This study reveals the importance of understanding the underground brittle-to-ductile behaviour of hydraulic fracture prior to the field implementation.

1. Introduction

The deformation of geo-materials incorporate the process as shear stress is increased toward failure: I- initial elastic deformation; II – non-recoverable deformation, i.e., brittle micro-cracking, or ductile/plastic flow; III – micro-cracks nucleation and macroscopic fracture propagation. The three stages are highly influenced by the confinement of stress, a brittle-to-ductile transitional failure is thus expected and observed as the increase of confinement (Aharonov and Scholz 2019; Evans et al. 1990; Minaeian 2014; Nygård et al. 2006; Vachaparampil and Ghassemi 2017; Wong and Baud 2012; Zhang et al. 1993). However, much fewer studies focus on the transitional deformation induced by hydraulic fracturing emerging in a wide range of underground engineering applications. Hydro-mechanical force is the main driven mechanism for the propagation of hydraulic fracture and with the same analogy, such transitional failure is expected as the function of confinement. Deeply understanding this transitional deformation can facilitate not only theoretical/numerical modelling but also provide critical insights for field applications associated with hydraulic fracturing.

When hydraulic fracture initiates and propagates within geo-materials under *in-situ* stresses, three types of failure modes are often observed: mode-I (tensile), mode-II (shear), and mixed-mode-I and II (Economides and Nolte 1989; Gischig and Preisig 2015; Wu 2006). The stress anisotropy, fluid mechanics, natural fractures, and rock mechanical properties are recognized as the most influential factors in the failure mode (Papanastasiou 1997; Zhou et al. 2008; Zhang et al. 2009; Gischig and Preisig 2015; Li et al. 2020; Liu et al. 2020; Sarmadivaleh 2012; Wang 2019; Wang et al. 2013; Zeng et al. 2020; Yang et al. 2021; Liu et al 2022). Incorporating all these parameters in fracturing analysis is complicated to be achieved. Since the hydraulic fracture growth is a dynamic process where the damage is mainly accumulated adjacent to the tip within the process zone (Desroches et al. 1994; Elices et al. 2002; Garagash 2019; Ju et al. 2021; Liu and Lecampion 2021; Papanastasiou 1997), which allows an alternative way studying the fracturing process. Several studies demonstrated that the plastic yielding/stress softening at the tip will absorb the effective injection energy, which significantly hinders the fracture propagation and results in a uniformed fracture geometry in ductile rocks (Feng et al. 2020; Ju et al. 2021; Papanastasiou 1997; Parisio et al. 2021).

Recently, Ju et al. (2021) performed a 3D numerical model for hydraulic fracture propagation in tightly brittle and ductile reservoirs. They confirmed that the stress concentration near the fracture tip is highly accommodated in the ductile reservoir. Parisio et al. (2021) carried out an experimental study of the brittle-to-ductile transition of hydraulic fracture within Polymethyl Methacrylate (PMMA). They observed complex fracture patterns under non-uniform stress distribution in the sample under the brittle regime. The complexity of fracture is significantly reduced as the ductility is increased. These studies revealed that a brittle-to-ductile transition is anticipated for the hydraulic fracture in a wide range of rock types in elevated confinements. However, such experimental study on a wide range of geo-materials is still lacking, which is essential to provide the data set required for the calibration of the modelling suitable for field applications.

In this paper, we present hydro-mechanical data based on hydraulic fracturing tests on variable types of geomaterials subjected to two sets of true triaxial stress conditions (TTSC), i.e., low confining (σ_1= 6.5MPa, σ_2= 3MPa, and σ_3=1.5MPa), and higher confining stresses (σ_1= 15MPa, σ_2=10MPa, and σ_2=5MPa); the evolution of wellbore pressure and the three mutually orthogonal strains induced by hydraulic fracture propagation are interpreted. We also interpreted the geometry and surface area (A_F) of hydraulic fracture based on the visualization of the X-ray Computational Tomography (CT) images of tested samples. These quantifications allow us to correlate the A_F and the brittleness index (BI) of the samples subjected to hydraulic fracturing; this correlation is compared against the previous numerical study. Viscoelastic stress relaxation of the tested materials is also conducted to explain the distinct geometry of hydraulic fracture subjected to the stress state.

2. Experimental Procedure

The six types of samples (see details of sample preparation and rock characterization in **Appendix A**) are used for rock mechanical, creep, and the hydraulic fracturing experiments under true triaxial stress conditions. Honey is used as fracturing fluid due to its Newtonian behavior. A micro-metering needle valve V_i is added to the injection inlet to restrict the flow rate when the rock breakdown takes place (Bunger 2005; Sarmadivaleh 2012). The experiments consist of three main components (**a**-pumping system; **b**-fracturing system **c**-data acquisition system) and are conducted in the following steps (**Fig.2)**:

(i) The cubic samples are initially loaded into the cell (**Fig.2b**), where the injection tube glued into the wellbore is connected to the injection line of the fracturing fluid.

(ii) The confining stresses are simultaneously elevated to a target value (at low confining case of σ_V = 6.5 MPa (940psi), σ_H = 3 MPa (440psi), σ_h = 1.5 MPa (220psi) or the higher case of σ_V = 15 MPa (2175psi), σ_H = 10 MPa (1450psi), σ_h = 5 MPa (725psi)): all stresses elevated to minimum stress, then two bigger stresses raised to the intermediate level, finally, the maximum stress is reached on one side, i.e., the loading rate is sufficiently small and constant to avoid any premature cracks induced by stresses. Waiting for at least 12hrs to ensure the stresses reach an equilibrium state, which also allows the time-dependent deformation (creep) has been fully developed prior to the initiation and propagation of the hydraulic fracture.

(iii) Vacuuming the injection line before injecting the honey into the wellbore (**Fig.2a**); monitoring the wellbore pressure for 1 hr when it reached a constant vacuum pressure value of -14 psi.

(iv) Start to inject the fracturing fluid into wellbore; start to monitor the wellbore pressure and 3D strain at the same time.

After the fracturing tests are completed, all samples are scanned a 3D X-ray Computed Tomography (XCT) image at a voxel resolution of 0.1 x 0.1 x 0.1 mm (Siemens SOMATOM Definition AS, set for helical scanning at 140 kV/500 mA) (Liu et al. 2022) were produced to document the geometry of hydraulic fractures within the samples. All quantities from CT images are interpreted by Avizo software.

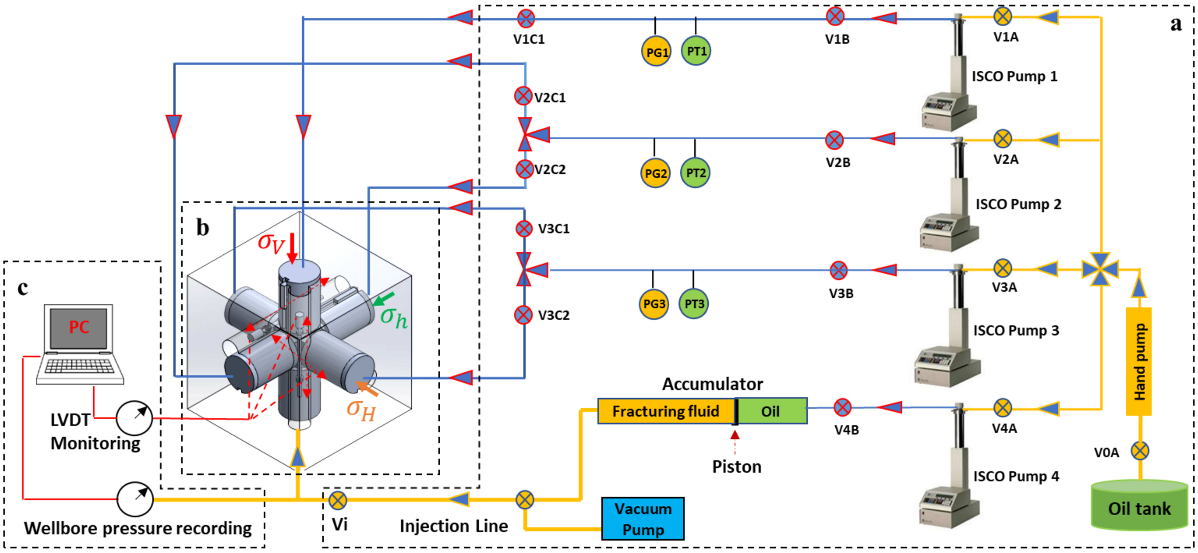

Fig.2 Schematic of hydraulic fracturing experimental setup: **a** Pumping system; **b** fracturing system; and **c** data acquisition system. *PT* pressure transducer, *PG* pressure gauge, V valve, Vi micro-meter valve, LVDT Linear Variable Differential Transformer, PC data acquisition.

3. Results

The representative hydro-mechanical results for tested samples (S_1-S_6) under low and high confinement are presented in **Section 3.1**; We also discuss the characteristics of intermediate strain (ε_H) induced by hydraulic fracture propagation (**Section 3.2**). Moreover, the geometry of hydraulic fracture subjected to both confinements are presented (**Section 3.3**). Finally, the correlation between fractured area and brittleness index (BI) is reported in **Section 3.4**. According to the quantification of brittleness index (BI) (Feng et al (2022)) and the failure characteristics of samples subjected to triaxial compression tests (**Figs.A2 and A3**), the six types of samples are classified into: brittle PMMA (BI=0.97), semi-brittle quartz-rich S_1

(BI=0.68), semi-brittle mixed-average S_4 (BI=0.57), semi-ductile calcite-rich S_3 (BI=0.44), the ductile clay-rich$_2$ S_5 (BI=0.38) and clay-rich S_2 (BI=0.35) under the low confinement. The same classification with different BI values under higher confinement: PMMA (BI=0.94), S_1 (BI=0.35), S_4 (BI=0.26), S_3 (BI=0.24), S_5 (BI=0.14), and S_2 (BI=0.09).

3.1 Hydro-mechanical data

Figs.3 and **4** show the representative hydro-mechanical data (i.e., the wellbore pressure and 3D strain (volumetric) induced by hydraulic fracturing) subjected to low (**Fig.3**) and high (**Fig.4**) confinement for the different samples: brittle PMMA (**Fig.3a and 4a**), semi-brittle S_1 (**Fig.3b and 4b**), semi-brittle S_4 (**Fig.3c and 4c**), semi-ductile S_3 (**Fig.3d and 4d**), ductile S_5 (**Fig.3e and 4e**), and S_2 (**Fig.3f and 4f**). The variation of 3D strain prior to the breakdown (maximum) pressure remains constant comparing to the strain after the breakdown pressure. The minimum horizontal strain ε_h is mainly produced by the propagation of fracture (negative ε_h in green curve), whereas the positive vertical strain ε_V (blue) indicates the vertical compression induced by the vertical stress. For brittle PMMA, and semi-brittle rock S_1, the strain ε_h abruptly increases after the (breakdown pressure) (**Figs.3 and 4a and b**); in contrast, for the ductile rock (S_5 and S_2), the ε_h are gradually increased to the peak value (**Figs.3 and 4e and f**).

Interestingly, the magnitude of strain ε_H along the intermediate horizontal stress σ_H (orange curve) shows a slightly negative deflection (tension) for semi-brittle sample S_1 under both low (**Fig.3b**) and high confinement (**Fig.4b)**; a slightly postive deflection (compression) for ductile sample S_2 under low confinement (**Fig.3f**) but a significantly postive deflection (compression) of ε_H is observed for S_2 under high confinement (**Fig.4f**). The more specific characteristics of intermediate strain ε_H will be discussed in **Sections 3.2 and 4.2**. Another important observation is the coincidence of the intermediate (ε_H) and vertical (ε_V) strain for semi-ductile S_3 (**Fig.4d**), ductile S_5 (**Fig.4e**) and S_2 (**Fig.4f**) subjected to the high confinement, which would be discussed in **Section 4**.

The volumetric strains (ε_T) are correspondingly shown at top right conner (purple curve) for each test. Under the low confinement (**Figs.3**): i) for brittle PMMA (**Figs.3a**), and semi-brittle sample S_1(**Figs.3b**), the volumetric strain ε_T are abruptly increased to the maximum value (negative deflection) after the period of constancy, indicating a significant dilated behaviour; ii) for semi-brittle samples S_4 (**Figs.3c**), and semi-ductile sample S_3 (**Figs.3d**), the ε_T are more gradually developed (nonlinear dilated behaviour); iii) whereas for the ductile sample S_5 (**Figs.3e**) the ε_T keeps relatively constant from the initiation to the end of propagation; notably for ductile sample S_2 (**Figs.3f**), the positive deflection of ε_T indicates a compressive manner of the deformation subjected to hydraulic fracturing.

Under the high confinement (**Figs.4**): i) for brittle PMMA (**Figs.4a**), the volumetric strain ε_T shows a more significant negative deflection (relatively linear after the breakdown) comparing to that under the low confinement; for semi-brittle sample S_1, the ε_T shows a significant negative deflection with strong nonlinearity (**Figs.4b**). ii) for semi-brittle S_4 (**Figs.4c**), semi-ductile S_3 (**Figs.4d**), and ductile samples S_5 (**Figs.4e**), the ε_T exhibits the analogous slightly negative deflection; ii) while for ductile sample S_2, volumetric strain ε_T is relatively constant from the early initiation until the end of propagation.

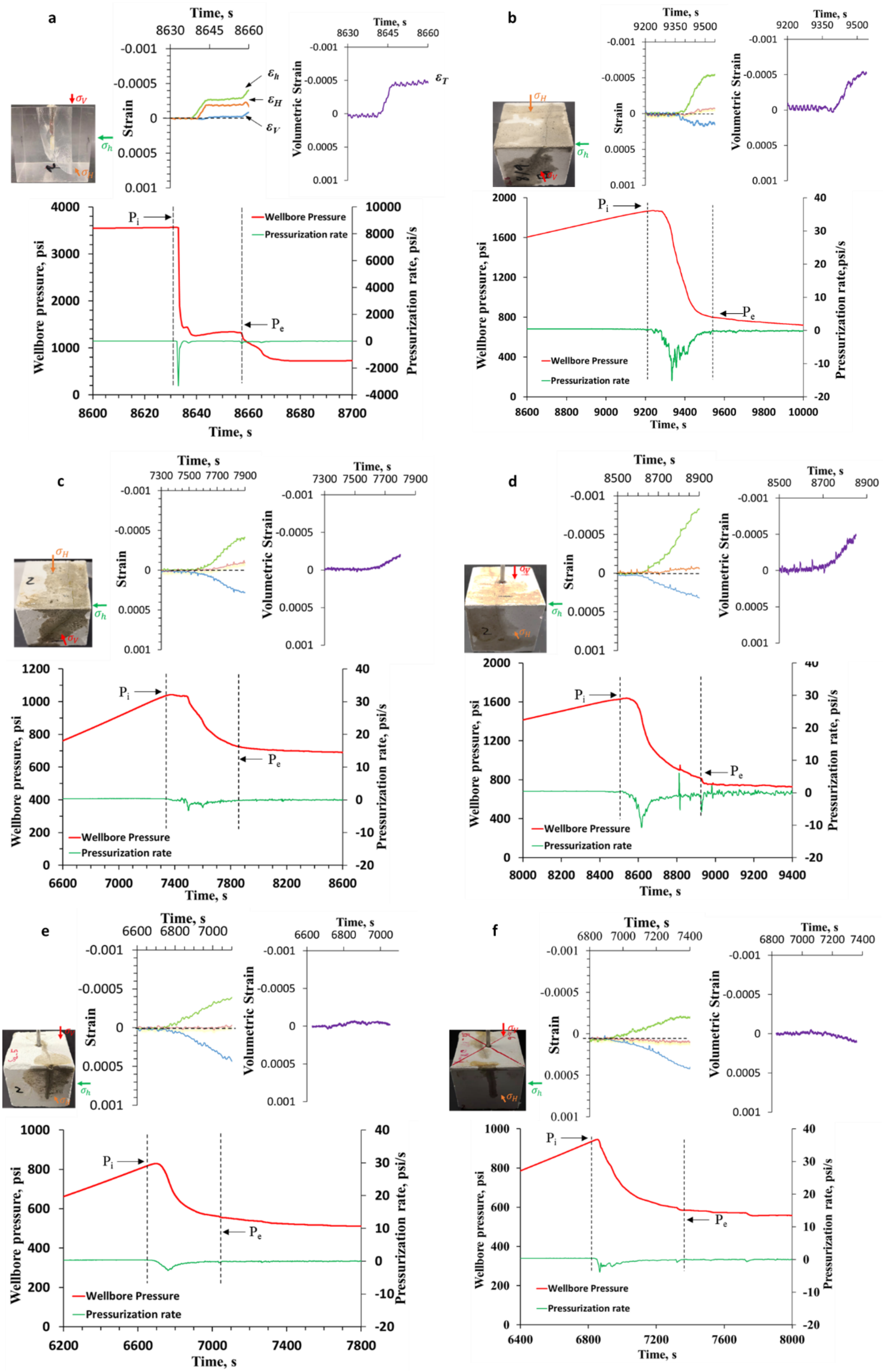

Fig.3 Synchronization of wellbore pressure and hydraulic fracture induced strain (vertical-ε_v, maximum horizontal (intermediate)-ε_H, and minimum horizontal-ε_h) under low confinement (6.5MPa , 3MPa, and 1.5MPa): a) PMMA2 b) S_1 c) S_4 d) S_3 e) S_5 f) S_2. P_i and P_e denote the borehole pressure at the initiation

and at the end of fracture propagation, respectively. The corresponding each sample after test are shown at the left. The volumetric strain (ε_v) are shown at the top-right.

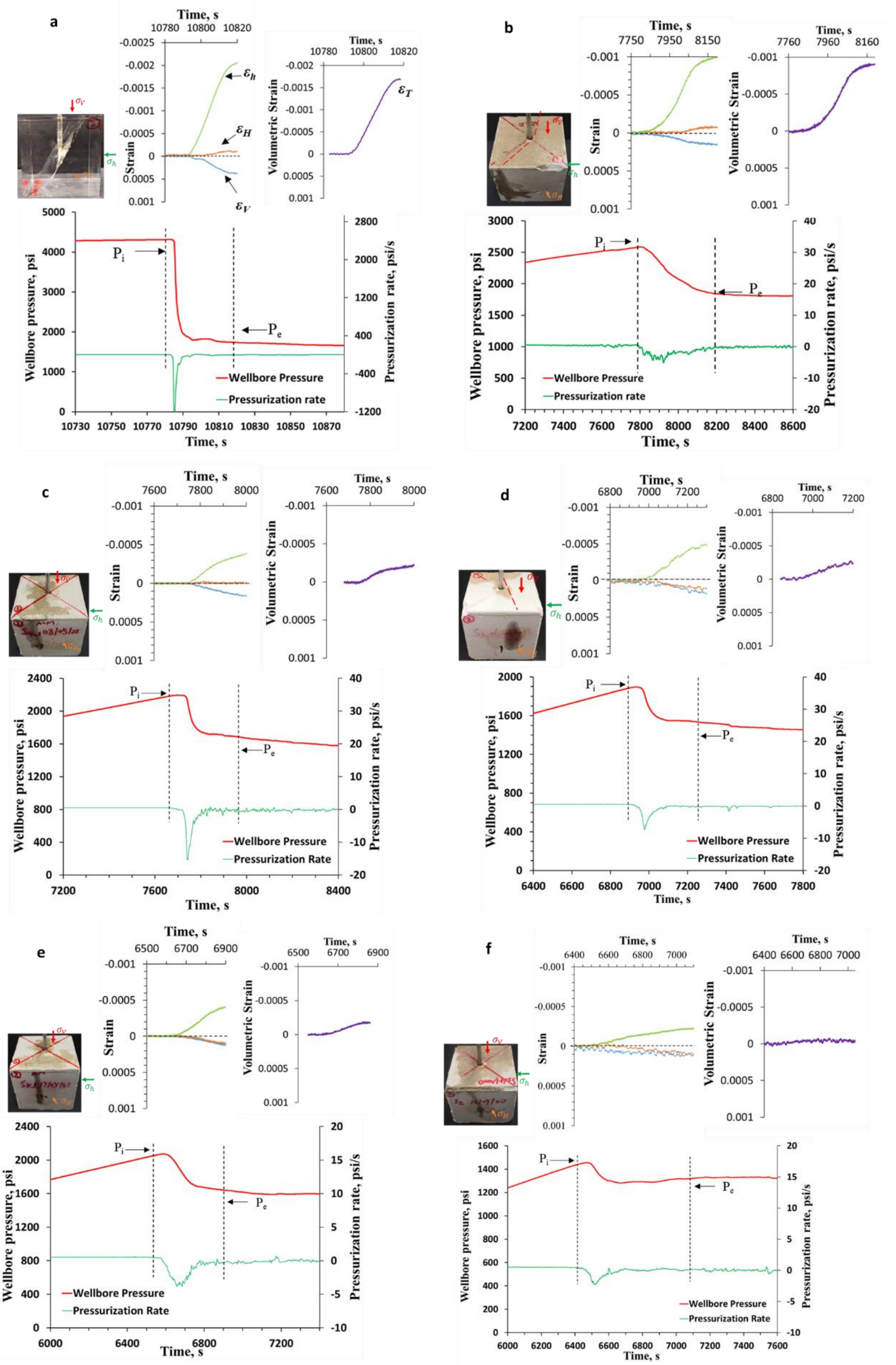

Fig.4 Synchronization of wellbore pressure and hydraulic fracture induced strain (vertical-ε_v, maximum horizontal (intermediate)-ε_H, and minimum horizontal-ε_h) under high confinement (15MPa , 10MPa,

and 5MPa): a) PMMA4 b) S_1 c) S_4 d) S_3 e) S_5 f) S_2. P_i and P_e denote the borehole pressure at the initiation and at the end of fracture propagation, respectively.The corresponding each sample after test are shown at the left. The volumetric strain (ε_v) are shown at the top-right.

3.2 Intermediate strain (ε_H) transition

Refer to the hydro-mechanical data set (**Figs.3 and 4**), the vertical strain ε_v shows a compression, and the minimum horizontal strain ε_h exhibits tension after breakdown pressure reaches for all samples. However, the characteristics of intermediate strain ε_H are highly variable, depending on the sample types and confinement (**Fig.5**). For semi-ductile S_3, and ductile samples S_5 and S_2 under higher confinement (**Fig.5b**), the magnitude of ε_H is significantly larger than that of lower confinement (**Fig.5a**). In summary, the significant transitions of ε_H from the brittle to ductile samples are observed:

Under the low confinement (**Fig.5a**): the intermediate strain ε_H shows a significant tensile deflection for brittle PMMA; a moderate tensile deflection for semi-brittle rock sample S_1 and S_4; a slight deflection for semi-ductile S_3; a nearly constant ε_H for ductile S_5; while a slight compressive deflection for ductile rock sample S_2. For the high confinement (**Fig.5b**), the transition is analogous to the lower one: the negative deflection of ε_H becomes ease for PMMA, and still exhibits the highest value among all samples; for the rock samples (from S_1 to S_5), the moderate negative deflection of ε_H are observed in semi-brittle rock sample S_1 and S_4 , but a significant positive compression of ε_H are found in semi-ductile S_3 , ductile S_5 and S_2.

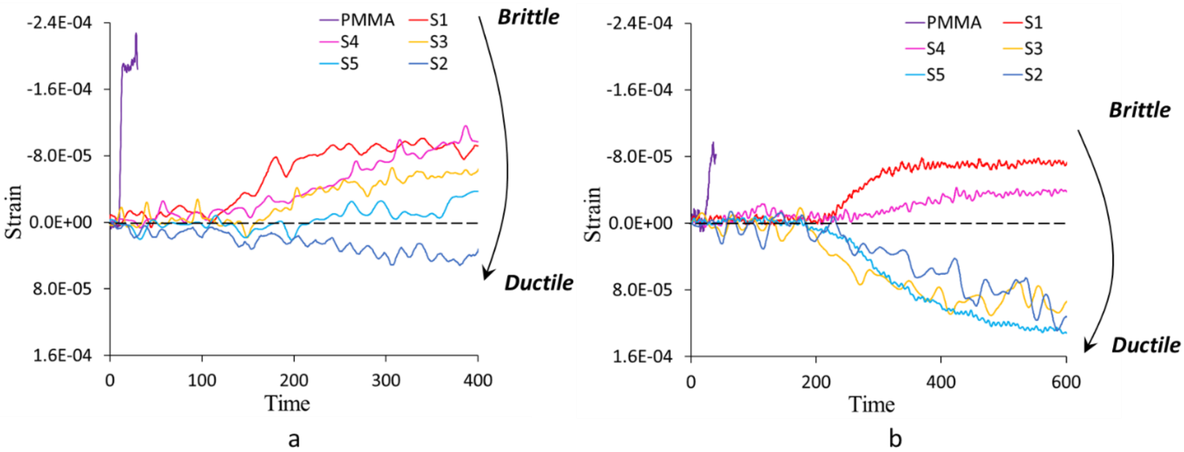

Fig.5 Transition of intermediate strain ε_H from brittle to ductile samples for a) low confinement b) high confinement

3.3 Geometry of Hydraulic Fracture

The geometry of hydraulic fracture for different samples subjected to low confinement (i.e., 6.5, 3 , and 1.5MPa) are shown in **Fig.6**. The fractures are highly tilted with respect to both σ_H and σ_h for brittle PMMA (**Fig.6a)**, and semi-brittle rock S_1 **(Fig.6b)** and S_4 **(Fig.6c)**. For the semi-ductile S_3(**Fig.6d**) and ductile rock S_5 (**Fig.6e**), the tilted angle are significantly reduced. In contrast, for ductile sample S_2 the fractures are nearly orthogonal to σ_h only (**Fig.6f**). Overall, it turns out a clear transition from highly titled (brittle) to orthogonal (ductile) fractures as the increase of ductility. This analogous phenomenon is also observed in the samples subjected to higher confinement (i.e., 15, 10 , and 5MPa) (**Fig.7**). The most interesting observation is the significant shear failure induced by hydraulic fracturing within PMMA: the geometry of hydraulic fracture (HF) is highly titled to ε_V and ε_h (**Fig.7a**), instead of inclining to ε_H and ε_h subjected to the lower confinement. Macroscopically, the geometry of hydraulic fractures are more planar/smooth under high confinement (**Fig.7**) rather than that of relatively tortuous fractures under the low confinement (**Fig.6**).

The experimental geometry of hydraulic fracture(HF) with respect to the brittle and ductile rocks (**Figs.6 and 7**) are in good agreement with the numerical study performed by Ju et al. (2021): for brittle reservoir the fracture is severely titled and result in a nonplanar geometry (**Fig.8a**), while for the ductile reservoir the inclination of fracture is highly mitigated due to the tip plasticity (**Fig.8c**), resulting in an axisymmetrically short fracture. Their numerical results are shown to be more consistent with our experimental geometry of HF subjected to the high confinement (**Fig.7**).

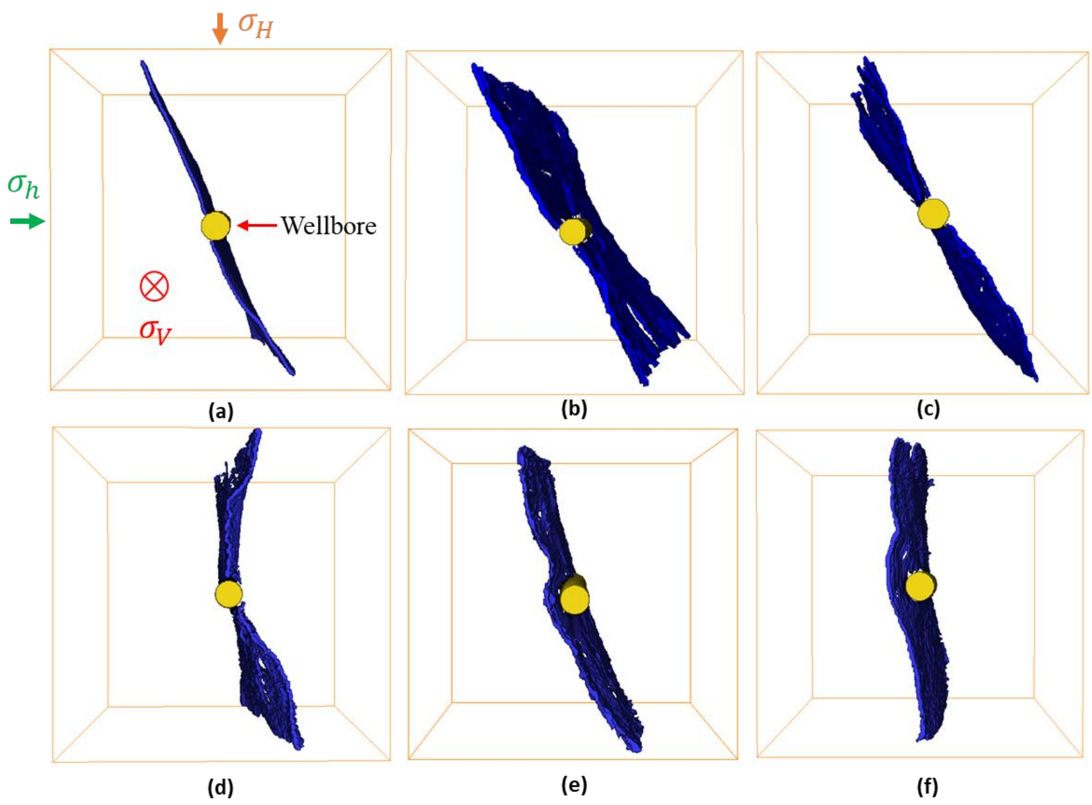

Fig.6. Geometry of hydraulic fracture from brittle to ductile transition a) PMMA b) S_1 c) S_4 d) S_3 e) S_5 f) S_2 under 6.5, 3.0, 1.5MPa

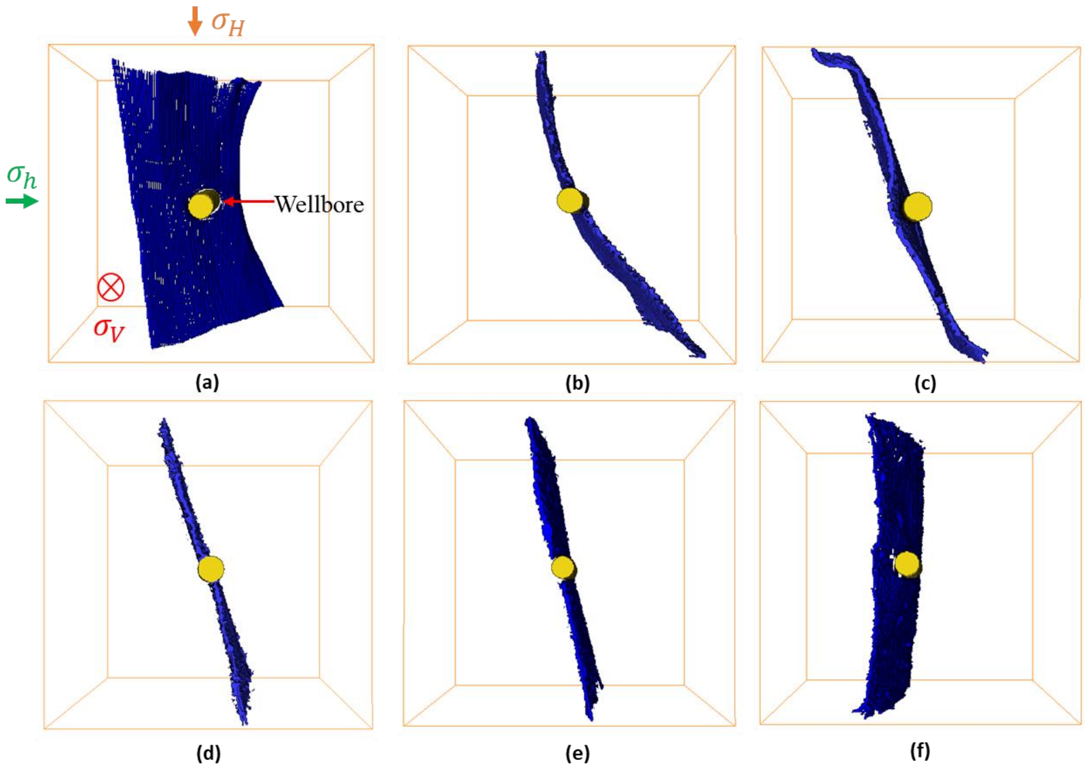

Fig.7. Geometry of hydraulic fracture from brittle to ductile transition a) PMMA b) S_1 c) S_4 d) S_3 e) S_5 f) S_2 under 15, 10, 5MPa

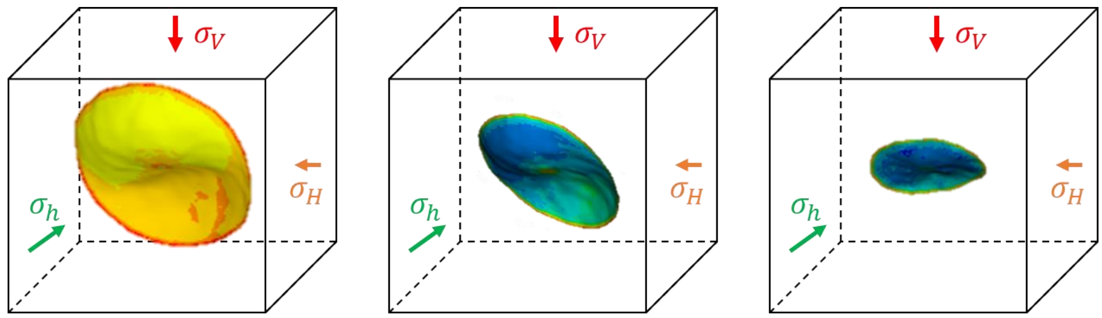

Fig.8. Numerical modelling of the morphology of hydraulic fracture from a) brittle, b) semi-brittle, and c) ductile reservoir under true triaxial stresses σ_v=30MPa, σ_H= σ_h=20MPa. Images modified from a 3D numerical work (Ju et al. (2021)).

3.4 Viscoelastic Stress Relaxation

In this section, we investigate the possible mechanisms for the distinct characteristics of hydro-mechanical deformation subjected to true triaxial stress states (i.e., **Sections 3.1 to 3.3**). Viscoelastic stress relaxation has been recognized as one of the primary reasons for higher magnitude of the minimum horizontal stress σ_h in unconventional shale gas reservoirs compared to the other layered clastic formations (Sone and Zoback 2014; Zoback, M. D., & Kohli, A. H. 2019; Mandal 2021).

The **Fig.9** illustrates how does the stress relaxation play a role in decreasing the stress anisotropy due to the increase of the magnitude of the least principal stress: as the significant increase of the minimum stress of the shale zone, the fracture growth is expected to be restricted. The creep compliance function based on power law model (among the constitutive models) has been accepted for sedimentary rock (Sone and Zoback 2014):

$$\varepsilon = \sigma B t^n \tag{4.1}$$

$$J(t) = B t^n \tag{4.2}$$

where J(t) is the creep compliance function described by axial strain ε(t) per unit value of differential stress σ; B and n are the fitting parameters referred to the creep constitutive parameters: B is the instantaneous elastic compliance in response to a unit stress step loading, n is the time-dependent exponent reflecting the rate of creep. These two parameters can be obtained based on the fitting of the creeping data shown in **Fig.B1**.

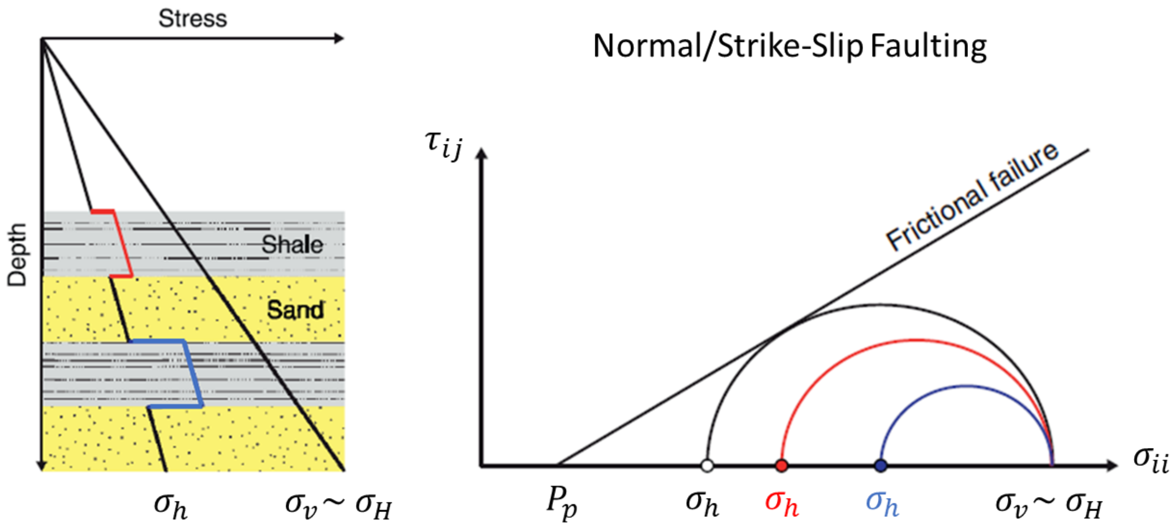

Fig.9 Schematic diagram illustrating how viscoelastic stress relaxation results in decreasing stress anisotropy due to increasing the magnitude of the least principal stress. Left: greater increment of S_{hmin} for the shale zone below rather than the minor increase of the S_{hmin} above the sand zone, which provide a barrier for fracture growth. Right: The Mohr-circle diagram in response to the viscoelastic stress relaxation (modified from Zoback, M. D., & Kohli, A. H. (2019)). Note the minimum horizontal stress $\sigma_3 = \sigma_h$ in this schematic.

Fig.10 shows the amount of different stress would be remained on the samples (PMMA, S_1 to S_5) after one-day from application of a one-dimensional strain step of 0.02. This value is selected based on our axial strain data of our samples under both triaxial (**Fig.A3**) and true-triaxial compressive tests (**Fig.B1**). The contour lines represent the predicted reciprocal stress relaxation after one-day with the strain step (Error! Reference source not found.): the highest magnitude of contour (e.g.,100MPa) indicates the stress accumulation is much faster than stress relaxation caused by viscoelastic deformation, which is usually observed in brittle rocks (Zoback, M. D., & Kohli, A. H. 2019); while the lowest magnitude of contour (e.g.,10MPa) reveals that the stress accumulation is much lower than the viscoelastic stress relaxation, which is evident in ductile rocks (Zoback, M. D., & Kohli, A. H. 2019). The contours intersected with the horizontal axis represents the purely elastic stress magnitude resulted from the strain. It can be seen that the samples-PMMA and S_1 are nearly located at the contour with the highest differential stress (100MPa), while the sample S_2 is at the lowest one (10MPa); and the samples S_3 ,S_4 , and S_5 are located in the between (from 30 to 40MPa). The repeatability of these results are shown in **Fig.10b**, although the difference are existed for the value of B and n (e.g., S_{2_2}, PMMA_2), the result of contour line shows the good repeatability. A clear brittle-to-ductile transition among our tested samples are indicated from this stress relaxation analysis. These results of viscoelastic stress relaxation not only explain the distinct characteristics of deformation among the tested samples (PMMA and S_1 to S_5) subjected to hydraulic fracturing (from **Fig.3 to Fig.7**), but also verified our BI prediction based on our recently proposed BI model (Feng et al 2022).

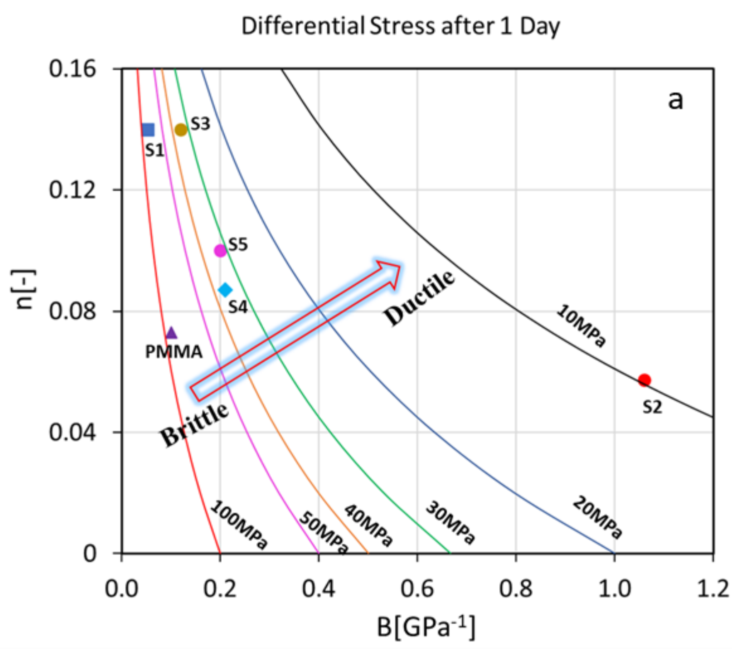

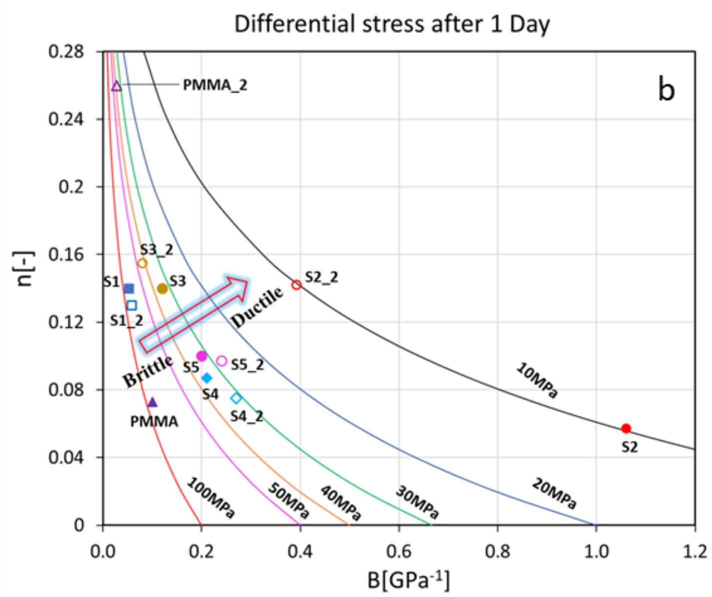

Fig.10 Differential stress response to change of the strain (0.02) for tested samples PMMA, and S_1 to S_5 after 1 Day under confinement of 15, 10, and 5MPa: a) representative stress relaxation results (see the creep data shown in **Fig.B1** b) full results of stress relaxation confirming the repeatability.

3.5 Fractured area verse BI

Ju et al. (2021) numerically studied the relation between fractured area and the brittleness index (BI) of shale reservoir. He showed that the fractured area is increased as the increase of BI. Here we quantify the hydraulic fractured area based on the CT images of tested rock samples (S_1 to S_5). We normalized the numerical (A_{TN}) and experimental fractured area (A_{FN}) based on the sample dimension, and plot both A_{TN} and A_{FN} verse BI (**Fig.11**). Both A_{TN} and A_{FN}

show an increased trend as the increase of BI. Notably, under the lower confinement, the fitting of A_{FN} and BI shows a second polynomial relation (negative coefficient). On the other hand, under the high confinement, the analogous second polynomial relation (positive coefficients) are observed for both A_{FN} and A_{TN} verse BI; but their quantities are significantly different.

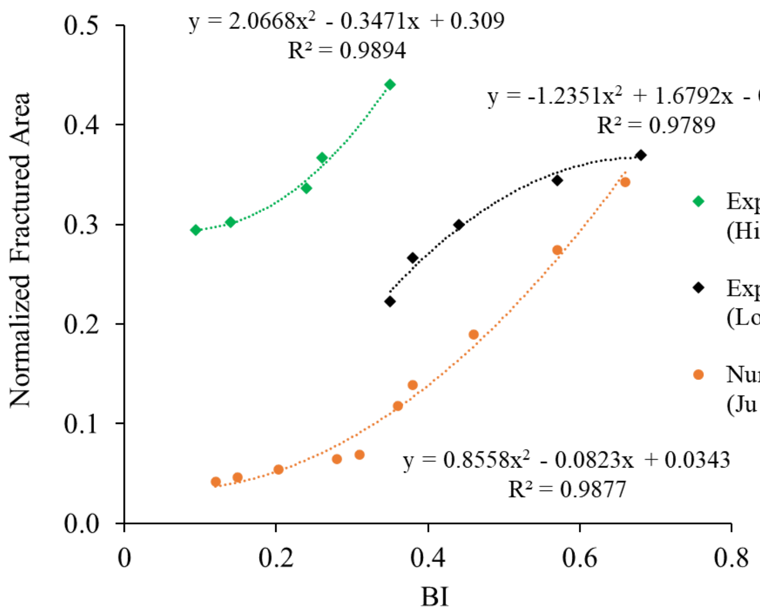

Fig.11 Normalized fractured area vs brittleness index (BI) based on our experimental results and literature data

4. Discussion and implementations

4.1 Deformation characteristics

The characteristics of hydro-mechanical deformation can be indicated by the 3D strain (vertical-ε_V, intermediate-ε_H, and minimum horizontal-ε_h), and the volumetric strain (ε_T). Under the lower confinement, for brittle PMMA (**Fig.3a**), and semi-brittle samples S_1 (**Fig.3b**) the volumetric strain and small portion of axial strain indicate the fracture deformation are relatively localized. On the other hand, for semi-brittle S_4 (**Fig.3c**), and semi-ductile S_3 (**Fig.3d**) the volumetric strain (ε_T) experiences more nonlinearity; while for ductile samples S_5 (**Fig.3e**) and S_2 (**Fig.3f**), the relative constant or compressive ε_T reveal that nonlocalized (spatially extended) plastic deformation are expected to be developed during the fracture propagation within the sample. Under the higher confinement, the failure of PMMA(**Fig.4a**) is dominated by vertical shear dilation (PMMA), while for semi-brittle rock S_1 (**Fig.4b**) the lateral shear-tensile opening is dominated; the more pronounced strain is attributed to higher breakdown/net pressure. In contrast to the significantly dilated volumetric strain (ε_T) observed for PMMA and S_1, the volume of the samples are only slightly dilated for semi-brittle S_4 (**Fig.4c**), semi-ductile S_3 (**Fig.4d**), and ductile sample S_5 (**Fig.4e**); while it stay relatively constant for ductile sample S_2 (**Fig.4f**). These observations indicate that the plastic deformation are highly nonlocalized within semi-ductile S_3, and ductile samples (S_5 and S_2) where the compression of intermediate (ε_H) and vertical strain (ε_V) are highly coincided (**Figs.4d,e, and f**). Such evidence of nonlocalized (spatially extended) plastic deformation induced by fracture propagation (stress/hydraulic) are also observed and proven in the numerical/experimental studies (Brantut et al. 2011; Huang and Chen 2021; Huang and Ghassemi 2016; Liu and Brantut 2022; Parisio et al. 2021; Ramos Gurjao et al. 2022; Richard et al. 2021; Schmidt et al. 2022; Tan et al. 2021; Vinci et al. 2014; Wrobel et al. 2022; Zhang et al. 2020).

4.2 Role of intermediate stress (σ_H) in hydraulic fracture

The intermediate stress σ_H is considered as an important parameter for the stress intensity factor (K_{HF}) if the geometry of hydraulic fracture (HF) is inclined to directions of both horizontal stresses (**Eqs.C6 to C8**), which is often observed in the laboratory or field (Sarvaramini et al. 2019; Yu et al. 2022). The previous studies demonstrated the significant role of σ_H in the mechanical properties, and associated failure modes induced by the elevated mechanical stresses on sandstone and shale (Minaeian 2014). In this study, the intermediate strain ε_H induced by the coupled hydraulic and mechanical force are highly variable regarding the sample types, and the confinement. The deflection of ε_H exhibits a clear brittle-to-ductile transition among the tested samples especially for the higher confining case (**Fig.5**). Noteworthily, for semi-ductile and ductile samples subjected to the higher confinement, the ε_H are significantly compressive after the early initiation stage (i.e., 200s), then starts to coincident with the vertical strain (ε_V) (**Figs.4d,e and f**). This observation can be explained by the more pronounced nonlocal (spatial extend) deformation induced by hydraulic fracture in the semi-ductile/ductile samples subjected to higher confining stresses (as discussed in **Section 4.1**).

4.3 Geometry of hydraulic fracture

The representative transitional geometry of hydraulic fracture (HF) for brittle and ductile samples **(Figs.6 and 7)** are in good agreement with the numerical study **(Fig.8)** performed by Ju et al. (2021). The mechanisms behind these interesting observations are worthily to be discussed. In this section, we will concentrate on the possible mechanisms leading to the more representative geometry under the higher confinement (i.e., 15, 10, and 5MPa)(**Fig.7**).

Fig.12 shows a typical shear failure induced by true tri-axial stresses compression (TTSC) i.e., $\sigma_V > \sigma_H > \sigma_h$ (Minaeian 2014; Rahjoo and Eberhardt 2021). Prior to this failure, a fictitious weak plane (normal faulting regime) is anticipated within the sample subjected to the stresses (**Fig.12**). Noteworthily, this fictitious plane is distinct from the weakest plane for propagation of a hydraulic fracture (i.e., the one perpendicular to minimum horizontal stress). Based on the geometry observed in our tested samples **(Figs.6 and 7)**, the representative schematic of brittle to ductile transition for the hydraulic fracture subjected to the stress regime displayed in **Fig.12**.

For the brittle PMMA the HF propagates along to the normal faulting regime (**Fig.7a, Fig.12,** and **Fig.13a**), which is mainly attributed to **(i)** the energy effectively converted from highly pressurized fracturing fluid causes high stress concentration near the crack tip (higher K_I (P_f) in **Eq.C7**), and **(ii)** the higher stress anisotropy accumulated from the principal stress magnitudes (**Fig.10**). While for semi-brittle rocks S_1 and S_4, the vertical shearing failure observed in PMMA is highly eased, instead, the hydraulic fracture is mainly inclined to both intermediate stress σ_H and the least principal stress σ_h (**Figs.7b** and **c, Fig.13b**). Compared to the HF geometry of brittle PMMA, the alleviation could be attributed to: **(i)** the slightly mitigated stress concentration near the fracture tip (K_I (σ_{coh}) in **Eq.C7**) due to the strain softening (Ju et al. 2021; Papanastasiou 1997) and **(ii)** the slightly reduced stress anisotropy due to the viscoelastic stress relaxation. On the other hand, for semi-ductile (S_3), and the ductile samples (S_5 and S_2), the HF is nearly perpendicular to the least principal stress σ_h (**Fig.13c** and **d)**. This is attributed to **(i)** the significant tip plasticity and softening behaviour highly reduce the stress concentration (Feng et al. 2020; Ju et al. 2021; Papanastasiou 1997), which significantly reduces the kinematic energy transformation from the accumulated injection energy (lower K_{HF} in **Eq.C7**); and **(ii)** the significant viscoelastic stress relaxation causes the increase of the least principal stress (**Fig.10**), resulting in more isotropic stress magnitude in these ductile formations (Zoback, M. D., & Kohli, A. H. 2019).

The abovementioned mechanisms (e.g., crack tip plasticity, viscoelastic stress relaxation) clearly explain why the geometry of hydraulic fracture always propagated along the theoretical weakest plane in semi-ductile/ductile samples, i.e., nearly perpendicular to the minimum horizontal stress **(Fig.13c** or **d)**, without being significantly affected by the fictitious weak plane induced by the deviatoric stress state ($\sigma_V > \sigma_H > \sigma_h$) shown in **Fig.12**. Notably, for the materials (S_1 to S_5) tested in this study, the macroscopic geometry of hydraulic fractures subjected to high confinement **(Fig.7)** are more planar than that of low confinement **(Fig.6)**, which is attributed to the higher resistance of fracture propagation as the increase of confinement/ductility.

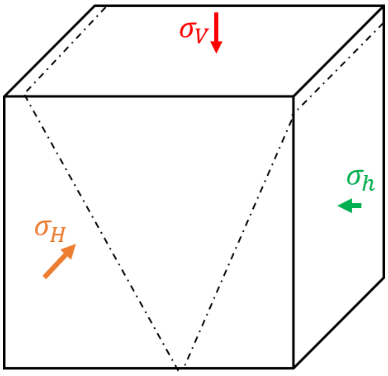

Fig.12 The failure mode of brittle materials under true triaxial stress compression i.e., $\sigma_v > \sigma_H > \sigma_h$ (Minaeian 2014; Rahjoo and Eberhardt 2021).

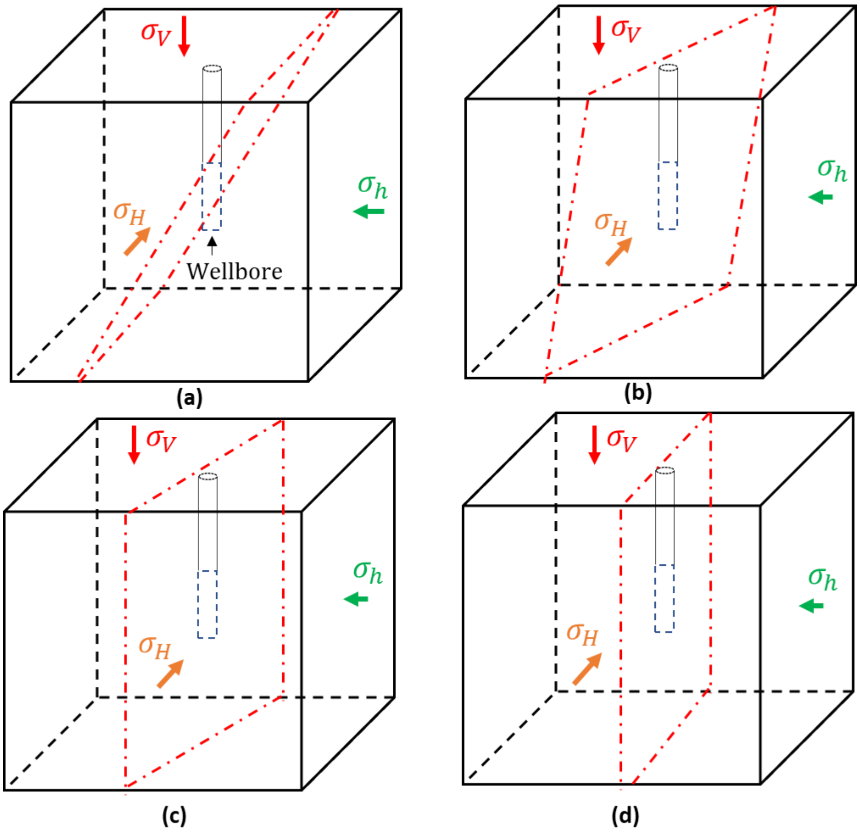

Fig.13 Representative Geometry of hydraulic fracture from brittle to ductile transition: **a)** brittle PMMA (under high confinement) **b)** brittle PMMA (under low confinement) or brittle/semi-brittle sample **c)** semi-brittle/semi-ductile sample **d)** ductile sample. Note: the failure plane shown above is a simplified diagram, not necessarily indicating the fracture will exactly follow that plane or penetrated to the boundary of sample.

4.4 Role of BI in Fractured area

laboratory results indicated that the fractured area (A_{FN}) are reduced from brittle to ductile samples subjected to both low and high confinement (**Fig.11**), which is in good agreement with the numerical study recently performed by Ju et al. (2021). As shown in **Fig.11**, the experimental results subjected to the high confinement (A_{FN} verse BI) shows an analogous polynomial relation comparing to the numerical results (A_{TN} verse BI); regardless of their quantities. For laboratory experiments, the limited sample size and continuously injected energy allow the fluid-driven fractures penetrate the boundary of sample; while the HF are retained within the boundary of numerical model due to the early termination of fracture propagation in ductile reservoirs (Ju et al. 2021).

Interestingly, for the same type of tested sample, the fractured area (A_{FN}) subjected to high confinement (15MPa, 10 MPa, and 5MPa) are larger than that of lower confinement (6.5MPa, 3 MPa, and 1.5MPa) (**Fig.11)**, although the brittleness index (BI) of former one is reduced. This could be attributed to: (i) higher deviatoric horizontal stress exerted on the samples subjected to high confinement (Van Dam and De Pater 1999; Van Dam et al. 2000). (ii) higher stress concentration near the fracture tip due to the higher breakdown/propagation pressure. This coupled mechanism causes the fracture to propagate in a manner of relatively higher effective stress and sufficient propagating time, resulting in a more tortuous fracture with relatively rougher surface in the view of meso-scale (**Fig.14**).

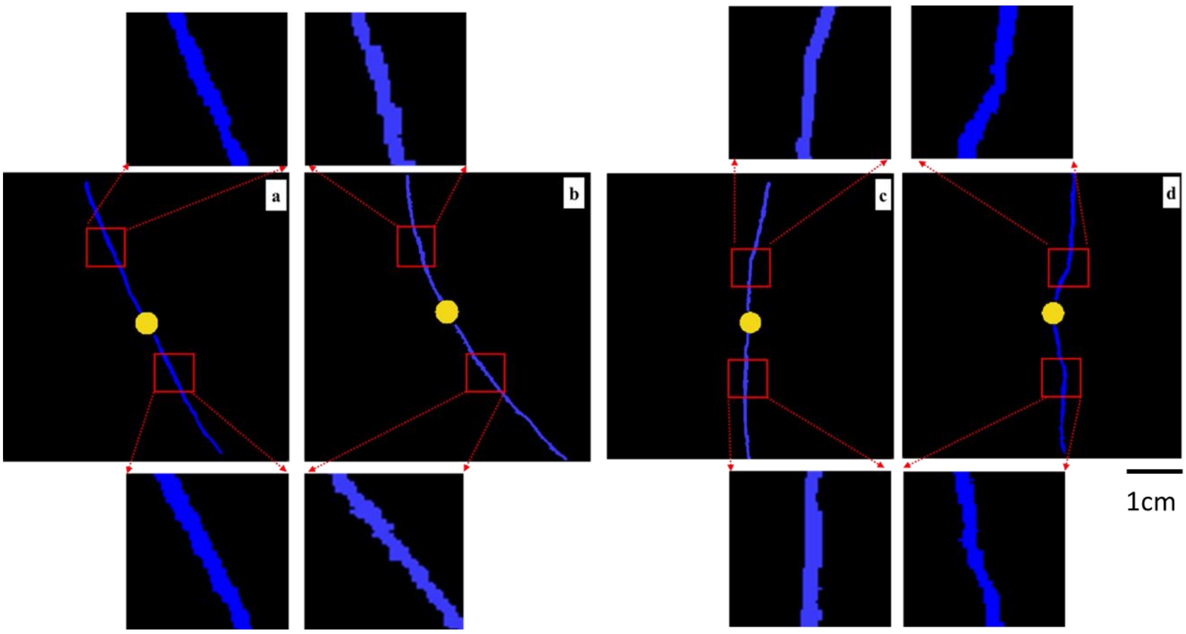

Fig.14 CT images of hydraulic fracture in semi-brittle rock S_1 under a) low and a) high confinement; ductile rock S_2 under c) low and d) high confinement

6. Conclusion

The initiation and propagation of hydraulic fractures in geomaterials plays an important role in geology (Weinberg and Regenauer-Lieb 2010), reservoir stimulation (Bakhshi et al. 2021; Huang and Chen 2021; Mandal et al. 2020), and the management of micro-seismicity (Amitrano 2003). However, the brittle-to-ductile transition of hydraulic fracturing process with depth has been rarely quantified in the laboratory despite its pivotal role for benchmarking field operations.

In this study, we conducted hydraulic fracturing experiments on five types of rock samples in addition to PMMA, which represents the extreme brittle reference. The samples were subjected to true triaxial stress conditions (TTSC), and during fluid injection wellbore pressure and the three-dimensional (3D) strains induced by hydraulic fracture propagation were simultaneously monitored. After each experiment the fractured sample was imaged using X-ray Computed Tomography (XCT); the 3D images were used to quantitatively evaluate the morphology and area of the induced hydraulic fracture (Avizo software). The analysis of stress relaxation based on creep data indicates the viscoelastic behavior should be considered for analysis of the stress state or deformation of different lithological layers in the field, rather than the simplified elasticity. These experiments are designed to shed light on the hydraulic fracturing response as a function of depth for a wide range of engineering applications. The following conclusions are addressed based on this study:

(i) The interpretation of the hydro-mechanical data (3D strain and volumetric strain (ε_T)) reveals the distinctive deformation characteristics for the brittle/semi-brittle, semi-ductile, and ductile samples. The non-localized (spatial extend) plastic deformation induced by hydraulic fracturing is pronounced in a semi-ductile sample (e.g., S_3), and a ductile sample (e.g., S_5 and S_2), especially for the higher confinement (**Figs.3 and 4**). In contrast, the fracture deformation is more localized dilation for the brittle PMMA (**Figs.3a and b)**, and the semi-brittle sample S_1 (**Figs.4a and b)**.

(ii) The intermediate stress (σ_H) may play a profound role in HF propagation and associated rock deformation: for the tested samples subjected to normal faulting regime (i.e., $\sigma_v > \sigma_H > \sigma_h$), the intermediate strain ε_H transits from tensile deflection to positive compression from the brittle to ductile samples; this phenomenon is enhanced as the increase of confinement (**Fig.5**).

(iii) The high-to-low inclined angle for hydraulic fractures (HFs) are observed from the brittle/semi-brittle to semi-ductile/ductile samples (**Figs.6** and **7**): For the brittle PMMA under the high confinement, extremely high stress concentration near the crack tip leads to a strong hydro-shearing fracture (**Figs.7a** and **13a**), which is consistent with the normal faulting regime **(Fig.12)**. For the semi-brittle samples (S_1 and S_4), the nonlocalized plasticity reduces the stress concentration near the fracture tip, inhibiting vertical hydro-shearing failure, instead, the horizontal hydro-dilating fractures are formed (see **Figs.7b and c; Figs.13b and c**). While for the semi-ductile sample S_3 and the ductile samples (S_5 and S_2), **(i)** the significantly nonlocalized plasticity reduces the near-tip stress concentration, which significantly reduces the effective propagation energy (Feng et al. 2020; Ju et al. 2021; Papanastasiou 1997; Parisio et al. 2021), allowing stress redistribution within the ductile rock surrounding the tip. **(ii)** the significant viscoelastic stress relaxation causes the increase of the least principal stress, resulting in more isotropic stress magnitude in these ductile formations **(Figs.9 and 10)**. These mechanisms are thought to be the key reasons of the highly mitigated inclination of hydraulic fractures observed in samples S_3 (**Figs.6d and 7d; Fig.13c**), S_5 (**Figs.6e and 7e; Fig.13c**), and the most significant-sample S_2 where hydraulic fracture is perpendicular to the minimum horizontal stress (**Figs.6f and 7f; Fig.13d**).

(iv) The measured surface area of the hydraulic fractures is reduced when transiting from the brittle to the ductile regime, regardless of the confinement (**Fig 13**), which is in good agreement with the numerical study reported by Ju et al. (2021). Notably, for the same type of sample under high confinement (15MPa, 10 MPa, and 5MPa), the fractured area (A_{FN}) is shown to be larger than that for lower confinement values (6.5MPa, 3 MPa, and 1.5MPa), despite the fact that the brittleness index (BI) is reduced when confinement is significantly higher. This is attributed to a more tortuous fracture with a relatively rougher surface at high confinement (**Fig 14**).

Declaration of competing interest

The authors declare that they have no known competing interest

Acknowledgments

The first author sincerely thanks China Scholarship Council- Curtin International Postgraduate Research Scholarship (CSC-CIPRS, Grant No. 201808190001) for their financial support on this research.

Appendix A: Test Materials and Mechanical properties

Synthetic rock blocks constituted of variable fractions of fine-grain quartz, kaolinite clay, calcite, and Standard Portland cement mixture (**Table A1**) are moulded. The PMMA were additionally used as an ideally homogeneous and brittle reference. More details on the fabrication procedures of block samples can be found in Sarmadivaleh and Rasouli (2015) and Feng et al. (2020). The prepared cubic/cylindrical blocks and the schematic of cubic sample assembly for a typical hydraulic fracturing test are shown in **Fig.A1**. In field, defects and stress concentrations play a role in hydraulic fracture propagating in mix-modes, i.e., non-perpendicular to the minimum principal stress (Parisio et al. 2021). To allow the stress concentration generating around the borehole, we design for drilling a 2/3 depth of the borehole (Feng et al. 2020; Parisio et al. 2021) (**Fig.A1**).The mechanical properties of prepared blocks are shown in **Table A2**. Details of the procedures for UCS and TCS testing used to determine these values can be found in Feng et al. (2020).

The physical photo of five new types of samples after Tri-axial compressive tests (TCS) are presented in **Fig.A2**. The shear failure is observed in Quartz-rich S_1 **(Fig.A2a)**, Average-mix S_4 **(Fig.A2b)** and Calcite-rich S_3 **(Fig.A2c)** samples, while for the two types of Clay-rich sample S_5 **(Fig.A2d)** and S_2 **(Fig.A2e)** there are no significant failure plane due to their high ductility under 3.4MPa of confinement. The representative stress-strain curve from TCS is shown in **Fig.A3,** in which the higher portion of plastic strain (axial/lateral) are observed in both clay-rich samples **(**S_2 and S_5).

Table A1. Composition and density of the five synthetic rock formulations (mineral cement mixtures) used in this study.

Mineral-cement mixture	Silica (%)	Kaolinite (%)	Calcite (%)	Cement (%)	Density(g/cm^3)
Quartz-rich(S_1)	52.5%	22.5%	0.0%	25%	1.58
Clay-rich(S_2)	22.5%	52.5%	0.0%	25%	1.26
Calcite-rich(S_3)	15.0%	7.5%	52.5%	25%	1.44
Mixed average(S_4)	30.0%	22.5%	22.5%	25%	1.50
Clay-rich$_2$(S_5)	30.0%	45%	0.0%	25%	1.46

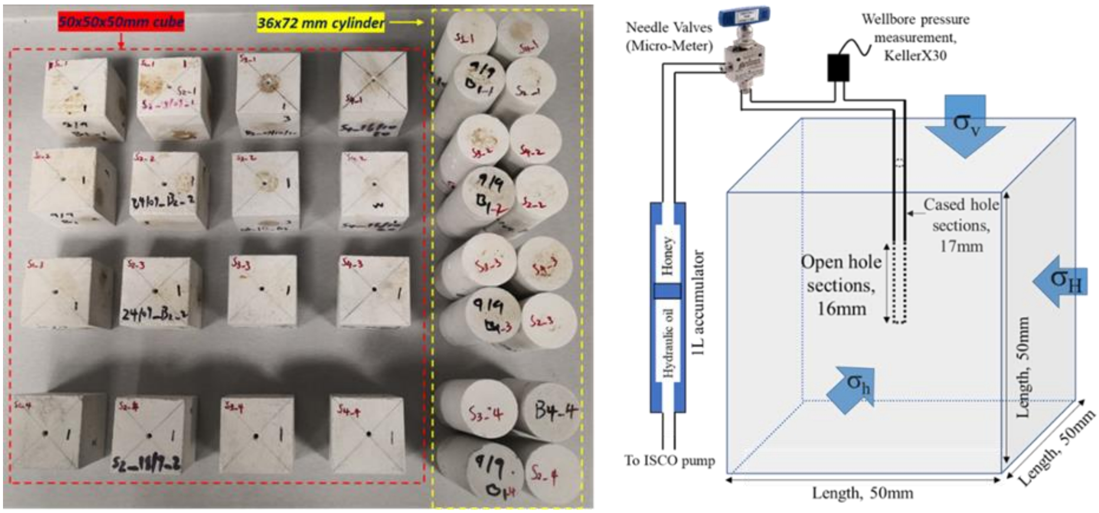

(a) (b)

Fig.A1 a) Part of the synthetic rock samples used in this study: a) 50x50x50mm cubes for hydraulic fracturing, and 36x72mm cylindrical plugs for mechanical characterisation; b) schematic of a typical cubic sample prepared for hydraulic fracturing tests (modified from Feng et al. (2022)).

Table A2. Mechanical properties of the mineral-cement mixtures and PMMA used in this study, and determined through unconfined (UCS) and triaxial (TCS) compression tests.

Mineral-cement mixture	Young's modulus E (GPa)	Poisson's ratio ν (-)	Friction angle Φ (°)	Cohesion C_O (MPa)	P-wave velocity V_P (km/s)	S-wave velocity V_S (km/s)	Porosity ϕ (-)
Quartz-rich(S_1)	6.9*	0.17*	42*	1.76*	2.1	1.4	0.29
Clay-rich(S_2)	2.6*	0.1*	35.3*	0.6*	1.3	0.87	0.3
Calcite-rich(S_3)	3.2*	0.21*	40.9*	0.9*	1.69	1.07	0.2
Mixed average(S_4)	3.0*	0.18*	35.8*	1.5*	1.8	1.17	0.24
Clay-rich2(S_5)	1.6*	0.17*	37.3*	0.8*	1.47	0.97	0.3
PMMA(S_6)	6.2**	0.39**	14.4**	44.6**	2.75	1.4	0

** UCS tests are conducted on dry samples, and TCS tests are conducted in dry conditions at 0.6, 2.1, and 3.4 MPa confining pressure.*
*** Data reported in the literature.*

a b c d e

Fig.A2 Failure patterns of the five new synthetic samples after TCS under confinement of 3.4MPa: a) Quartz-rich S_1 b) Average-mix S_4 c) Calcite-rich S_3 d) Clay-rich S_2 e) Clay-rich S_5

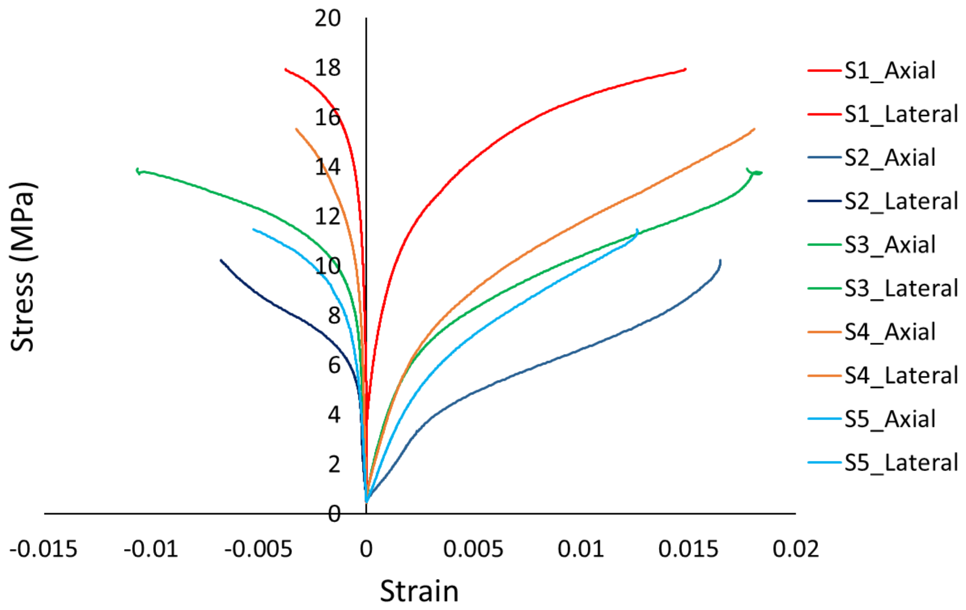

Fig.A3 Stress vs strain curve obtained from TCS testing on samples (S_1 to S_5)

Appendix B. Creep data used for stress relaxation analysis

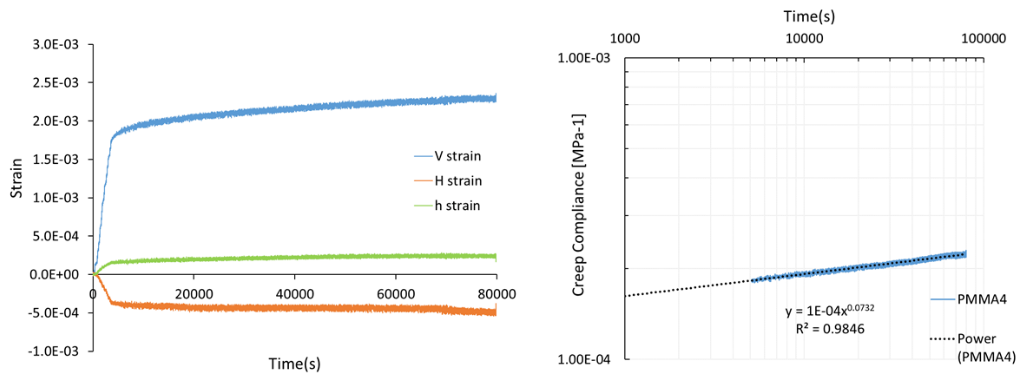

(a)

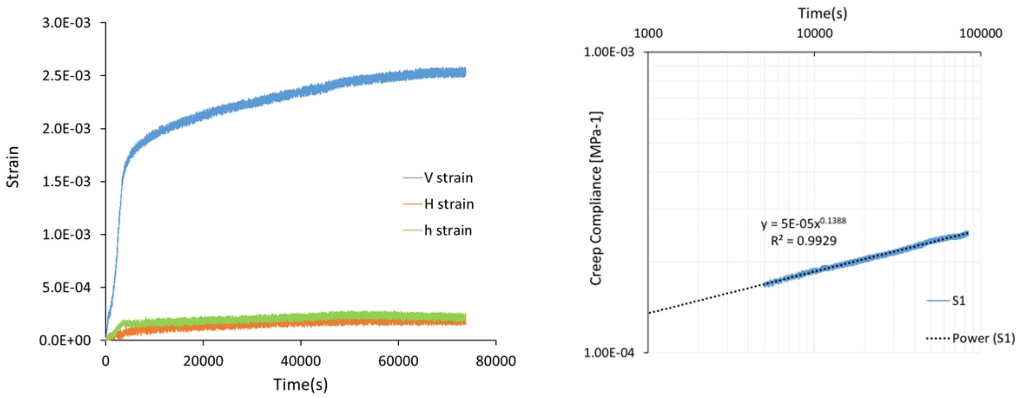

(b)

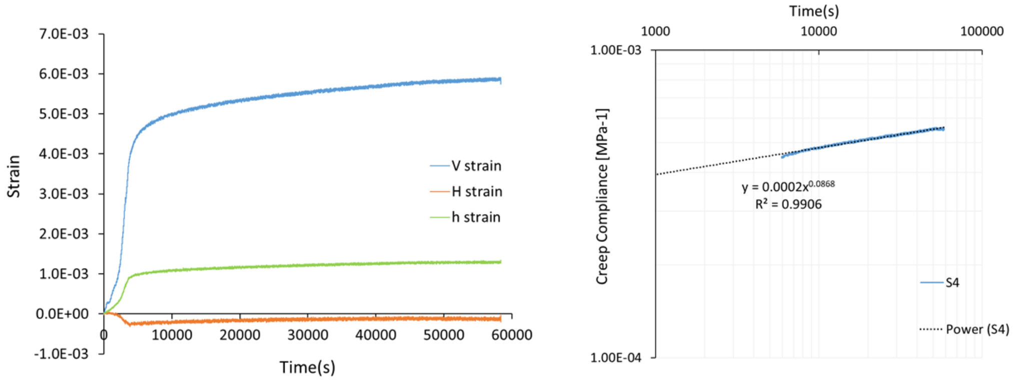
Strain
Time(s)
V strain
H strain
h strain
Time(s)
Creep Compliance [MPa-1]
y = 0.0002x^0.0868
R² = 0.9906
S4
Power (S4)

(c)

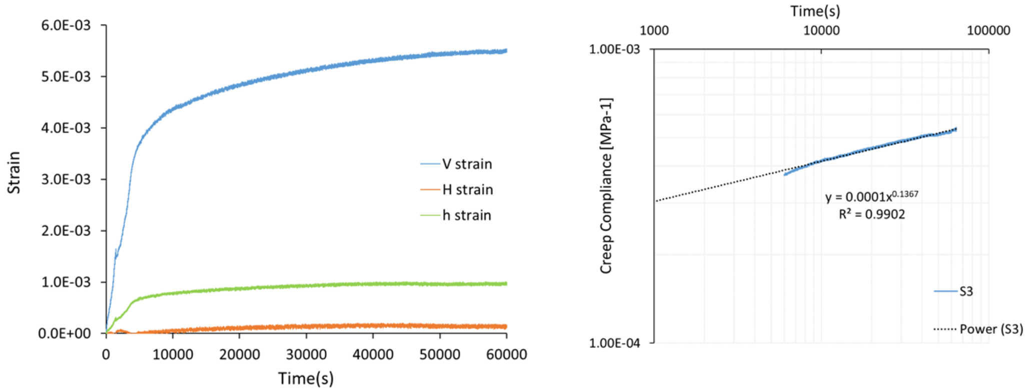
Strain
Time(s)
V strain
H strain
h strain
Time(s)
Creep Compliance [MPa-1]
y = 0.0001x^0.1367
R² = 0.9902
S3
Power (S3)

(d)

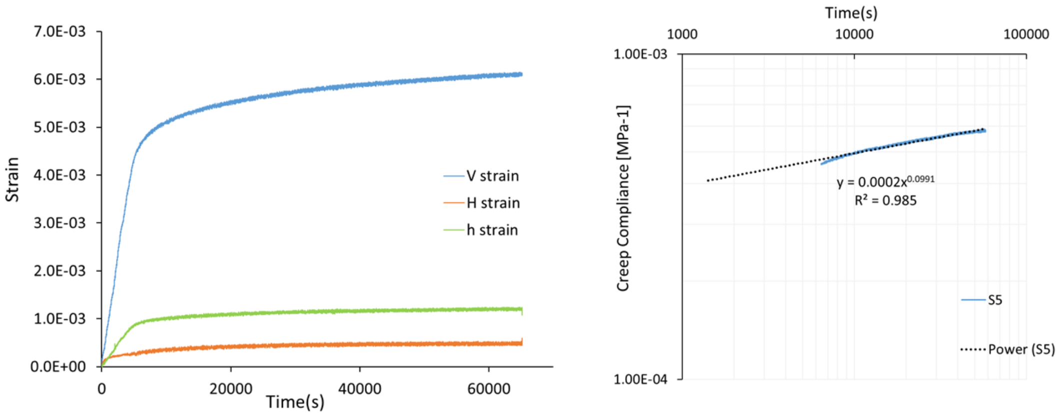
Strain
Time(s)
V strain
H strain
h strain
Time(s)
Creep Compliance [MPa-1]
y = 0.0002x^0.0991
R² = 0.985
S5
Power (S5)

(c)

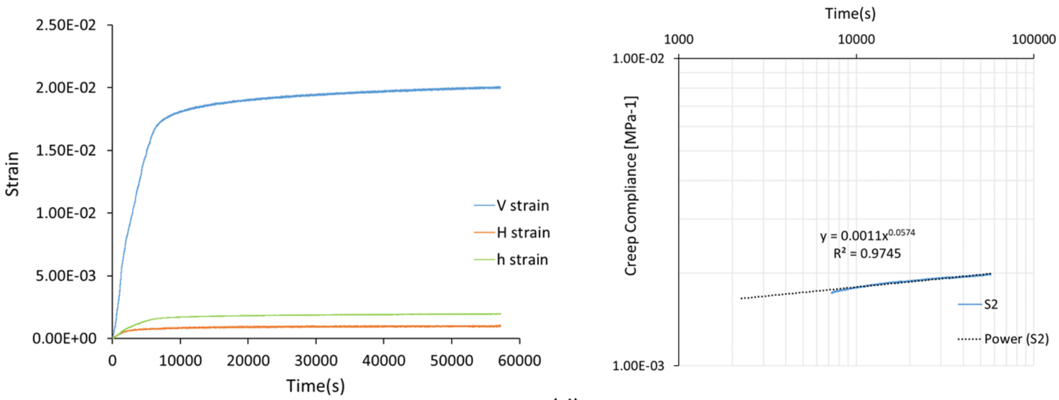
Strain
Time(s)
V strain
H strain
h strain
Time(s)
Creep Compliance [MPa-1]
y = 0.0011x^0.0574
R² = 0.9745
S2
Power (S2)

(d)

Fig.B1 Representative creep data (including the loading stage shown at the left) used for stress relaxation analysis for six type of the samples tested in this study: a) PMMA b) Quartz-rich S_1 c) Mixed-average S_4 d) Calcite-rich S_3 e) Clay-rich$_2$ S_5 f) Clay-rich S_2 under 15, 10, and 5MPa

Appendix C. Propagation Criterion for Hydraulic Fracture

Stress intensity factor (*K*) at the crack tip has been studied as an important parameter in linear elastic fracture mechanics (Irwin 1957). Later, Barenblatt (1962) and Dugdale (1960) proposed a well-known Barenblatt-Dugdale model, accounting for the nonlinear material behaviour into a small size of cohesive zone near the crack tip. Hillerborg et al. (1976) introduced a model for the finite cohesive zone, adapting to the propagation of a cohesive crack in elastic material when the tensile softening takes place (Boone et al. 1986; Desroches et al. 1994; Papanastasiou and Thiercelin 1993).

For propagating a penny-shaped hydraulic fracture (**Fig.C1**), the three aspects- (i) fluid pressure, (ii) *in-situ* stresses, and (iii) cohesive stresses are necessarily considered into the stress intensity factor (K_{HF}) (Lhomme 2005). The pressurized fracturing fluid provides a positive contribution to the stress intensity factor $K_I(P_f)$ reads:

$$K_I(P_f) = 2\sqrt{\frac{R}{\pi}}\int_0^{c_f} K_{np}(\xi, c)p_f(\xi, t)d\xi \qquad \text{(C1)}$$

Where P_f is the fluid pressure, R is the radius of fracture extent, R_f is the radius of fluid front (**Fig.C1**); $\xi=x/R_w$, $c=R/R_w$, and $c_f=R_f/R_w$ are the normalized length variables to borehole radius R_w; the kernel function $K_{np}(\xi,c)$ denotes the effect of wellbore geometry in stress intensity factor(Keer et al. 1977; Lhomme 2005; Nilson and Proffer 1984).

If we consider a hydraulic fracture subjected to the both horizontal stresses, i.e., minimum (σ_h) and intermediate (σ_H), the resultant normal stress on the fracture walls (σ_r) negatively contributed to the stress intensity factor $K_I(\sigma_r)$ reads:

$$K_I(\sigma_r) = -2\sqrt{\frac{R}{\pi}}\sigma_r\int_0^{c} K_{np}(\xi, c)d\xi \qquad \text{(C2)}$$

The inelastic behaviour can be modelled by tensile cohesive stresses exerted on the fracture wall within the cohesive zone (Elices et al. 2002; Garagash 2019; Lhomme 2005; Liu and Lecampion 2021), a degradation function f_{wct} is introduced to address the linear/nonlinear relation between the cohesive stress (σ_{coh}) and associated fracture opening (w) from the peak load to critical fracture opening (w_c):

$$\sigma_{coh} = \sigma_t f_{w_{ct}}, \; 0 < f_{w_{ct}} < 1 \;, \; w < w_c \tag{C3}$$

$$\sigma_{coh} = 0, \; w \geq w_c \tag{C4}$$

The cohesive stresses provided a negative contribution to the stress intensity factor K_I (σ_{coh}) reads as:

$$K_I(\sigma_{coh}) = -2\sqrt{\frac{R}{\pi}}\sigma_t \int_{c_v}^{c} K_{np}(\xi, c) f_{w_{ct}} d\xi \tag{C5}$$

Where R_v is the visible radius of the crack (**Fig.C1**); $c_v = (R_v - R_w)/R_w$

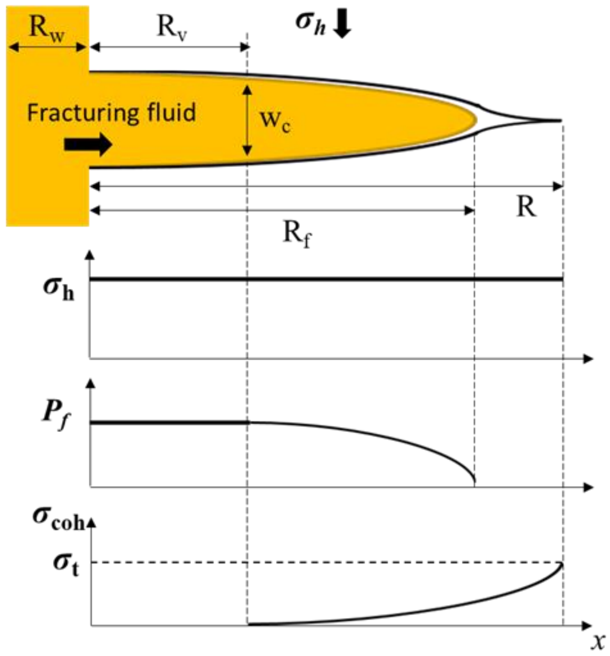

Fig.C1 Schematic of loading of a penny-shaped hydraulic fracture with fluid lag (Image modified from Lhomme (2005))

The summation of the three contributions (**Eqs.C1 to C3**) to the stress intensity factor (K_{HF}) for hydraulic fracture is necessarily to be equal to zero at the true crack tip, reads:

$$K_{HF} = K_I(P_f) + K_I(\sigma_r) + K_I(\sigma_{coh}) = 0 \tag{C6}$$

In order to propagate a hydraulic fracture, the K_{HF} must be larger than 0, reads:

$$\underbrace{2\sqrt{\frac{R}{\pi}}\int_0^{c_f} K_{np}(\xi, c) p_f(\xi, t) d\xi}_{K_I(P_f)} > \left[\underbrace{2\sqrt{\frac{R}{\pi}}\sigma_r \int_0^{c} K_{np}(\xi, c) d\xi}_{K_I(\sigma_r)} + \underbrace{2\sqrt{\frac{R}{\pi}}\sigma_t \int_{c_v}^{c} K_{np}(\xi, c) f_{w_{ct}} d\xi}_{K_I(\sigma_{coh})}\right] \tag{C7}$$

and reduces to:

$$\int_0^{c_f} K_{np}(\xi,c)p_f(\xi,t)d\xi > \left[\sigma_r \int_0^{c} K_{np}(\xi,c)d\xi + \sigma_t \int_{c_v}^{c} K_{np}(\xi,c)f_{w_{ct}}d\xi\right] \quad \text{(C8)}$$

It can be seen that both σ_r and σ_{coh} provide the resistance for initiation and propagation of a hydraulic fracture (HF). It is worthy to note that the intermediate stress σ_H may play an important role in K_I (σ_r) if the HF is inclined to the directions of both horizontal stresses. Therefore, the performance of σ_H and the intermediate strain ε_H induced by HF propagation are worthily to be monitored/evaluated (see **Section 3.2**). The cohesive stress σ_{coh} profoundly affect the propagation of a HF, especially for soft/ductile materials under stress field (Ju et al. 2021; Liu and Lecampion 2021; Papanastasiou 1997; Papanastasiou and Thiercelin 1993). If the different materials exhibit the same value of both K_I (P_f) and K_I (σ_r), the K_I (σ_{coh}) will be the dominated parameter differentiating the behaviour of fracture propagation.

Reference

Aharonov E, Scholz CH (2019) The brittle-ductile transition predicted by a physics-based friction law. Journal of Geophysical Research: Solid Earth 124:2721-2737

Amitrano D (2003) Brittle-ductile transition and associated seismicity: Experimental and numerical studies and relationship with the b value. Journal of Geophysical Research: Solid Earth 108

Bakhshi E, Golsanami N, Chen L (2021) Numerical modeling and lattice method for characterizing hydraulic fracture propagation: a review of the numerical, experimental, and field studies. Archives of Computational Methods in Engineering 28:3329-3360

Barenblatt GI (1962) The mathematical theory of equilibrium cracks in brittle fracture. Advances in applied mechanics 7:55-129

Boone T, Wawrzynek P, Ingraffea A Simulation of the fracture process in rock with application to hydrofracturing. In: International Journal of Rock Mechanics and Mining Sciences & Geomechanics Abstracts, 1986. vol 3. Elsevier, pp 255-265

Brantut N, Schubnel A, Guéguen Y (2011) Damage and rupture dynamics at the brittle-ductile transition: The case of gypsum. Journal of Geophysical Research: Solid Earth 116

Bunger AP (2005) Near-surface hydraulic fracture. University of Minnesota,

Desroches J, Detournay E, Lenoach B, Papanastasiou P, Pearson JRA, Thiercelin M, Cheng A (1994) The crack tip region in hydraulic fracturing. Proceedings of the Royal Society of London Series A: Mathematical and Physical Sciences 447:39-48

Dugdale DS (1960) Yielding of steel sheets containing slits. Journal of the Mechanics and Physics of Solids 8:100-104

Economides MJ, Nolte KG (1989) Reservoir stimulation vol 2. Prentice Hall Englewood Cliffs, NJ,

Elices M, Guinea G, Gomez J, Planas J (2002) The cohesive zone model: advantages, limitations and challenges.Engineering fracture mechanics 69:137-163

Evans B, Fredrich JT, Wong TF (1990) The brittle-ductile transition in rocks: Recent experimental and theoretical progress.The Brittle-Ductile Transition in Rocks, Geophys Monogr Ser 56:1-20

Feng R, Zhang Y, Rezagholilou A, Roshan H, Sarmadivaleh M (2020) Brittleness Index: from conventional to hydraulic fracturing energy model. Rock Mechanics and Rock Engineering 53:739-753

Feng R., Sarout J., Daustriat J., Ghuwainim Y., Rezaee R., Sarmadivaleh M (2022). Laboratory validation of a new hydro-mechanical energy-based brittleness index model for hydraulic fracturing. EarthArXiv preprint, DOI: doi.org/10.31223/X55M1J

Garagash DI (2019) Cohesive-zone effects in hydraulic fracture propagation. Journal of the Mechanics and Physics of Solids 133:103727

Gischig VS, Preisig G Hydro-fracturing versus hydro-shearing: a critical assessment of two distinct reservoir stimulation mechanisms. In: 13th ISRM International Congress of Rock Mechanics, 2015. OnePetro,

Hillerborg A, Modéer M, Petersson P-E (1976) Analysis of crack formation and crack growth in concrete by means of fracture mechanics and finite elements. Cement and concrete research 6:773-781

Huang C, Chen S (2021) Effects of Ductility of Organic-Rich Shale on Hydraulic Fracturing: A Fully Coupled Extended-Finite-Element-Method Analysis Using a Modified Cohesive Zone Model. SPE Journal 26:591-609

Huang K, Ghassemi A A coupled nonlocal damage model for hydraulic fracture propagation. In: 50th US Rock Mechanics/Geomechanics Symposium, 2016. OnePetro,

Irwin GR (1957) Analysis of stresses and strains near the end of a crack traversing a plate

Ju Y, Wu G, Wang Y, Liu P, Yang Y (2021) 3D Numerical Model for Hydraulic Fracture Propagation in Tight Ductile Reservoirs, Considering Multiple Influencing Factors via the Entropy Weight Method. SPE Journal:1-18

Keer L, Luk V, Freedman J (1977) Circumferential edge crack in a cylindrical cavity

Lhomme T (2005) Initiation of hydraulic fractures in natural sandstones

Li JX, Rezaee R, Müller TM (2020) Wettability effect on wave propagation in saturated porous medium.The Journal of the Acoustical Society of America 147:911-920

Liu D, Brantut N (2022) Micromechanical controls on the brittle-plastic transition in rocks. arXiv preprint arXiv:221111831

Liu D, Lecampion B (2021) Propagation of a plane-strain hydraulic fracture accounting for a rough cohesive zone. Journal of the Mechanics and Physics of Solids 149:104322

Liu Q, Xue L, Sarout J, Lin Q, Pan W, Liu Y, Feng R (2022) Automatic history matching of multistage fractured shale gas reservoir constrained by microseismic data. Journal of Petroleum Science and Engineering 213:110357

Liu S., Klaus T., Feng R., Bona A., Sarmadivaleh M (2022). Microstructure-based Modelling of Hydraulic Fracturing in Low-Permeability Rocks using the Cohesive Element Method. *Engineering Fracture Mechanics*, 108912.

Liu Y et al. (2020) Mechanical properties and failure behavior of dry and water-saturated anisotropic coal under true-triaxial loading conditions. Rock Mechanics and Rock Engineering 53:4799-4818

Mandal PP, Sarout J, Rezaee R (2020) Geomechanical appraisal and prospectivity analysis of the Goldwyer shale accounting for stress variation and formation anisotropy. International Journal of Rock Mechanics and Mining Sciences 135:104513

Mandal PP (2021) Integrated Geomechanical Characterization of Anisotropic Gas Shales: Field Appraisal, Laboratory Testing, Viscoelastic Modelling, and Hydraulic Fracture Simulation. Curtin University

Minaeian V (2014) True triaxial testing of sandstones and shales. Curtin University

Nilson R, Proffer W (1984) Engineering formulas for fractures emanating from cylindrical and spherical holes

Nygård R, Gutierrez M, Bratli RK, Høeg K (2006) Brittle–ductile transition, shear failure and leakage in shales and mudrocks. Marine and Petroleum Geology 23:201-212

Papanastasiou P (1997) The influence of plasticity in hydraulic fracturing. International Journal of Fracture 84:61-79

Papanastasiou P, Thiercelin M Influence of inelastic rock behaviour in hydraulic fracturing. In: International journal of rock mechanics and mining sciences & geomechanics abstracts, 1993. vol 7. Elsevier, pp 1241-1247

Parisio F et al. (2021) A laboratory study of hydraulic fracturing at the brittle-ductile transition. Scientific Reports 11:1-16

Rahjoo M, Eberhardt E (2021) Development of a 3-D confinement-dependent dilation model for brittle rocks; Part 1, derivation of a Cartesian plastic strain increments ratios approach for non-potential flow rules. International Journal of Rock Mechanics and Mining Sciences 145:104668

Ramos Gurjao KG, Gildin E, Gibson R, Everett M (2022) Investigation of Strain Fields Generated by Hydraulic Fracturing with Analytical and Numerical Modeling of Fiber Optic Response. SPE Reservoir Evaluation & Engineering 25:367-379

Richard D, Lerner E, Bouchbinder E (2021) Brittle to ductile transitions in glasses: Roles of soft defects and loading geometry. arXiv preprint arXiv:210305258

Sarmadivaleh M (2012) Experimental and numerical study of interaction of a pre-existing natural interface and an induced hydraulic fracture. Curtin University

Sarmadivaleh M, Rasouli V (2015) Test design and sample preparation procedure for experimental investigation of hydraulic fracturing interaction modes. Rock Mechanics and Rock Engineering 48:93-105

Sarvaramini E, Dusseault MB, Komijani M, Gracie R (2019) A non-local plasticity model of stimulated volume evolution during hydraulic fracturing. International Journal of Solids and Structures 159:111-125

Schmidt P, Dutler N, Steeb H (2022) Importance of fracture deformation throughout hydraulic testing under in situ conditions. Geophysical Journal International 228:493-509

Sone H, Zoback MD (2014) Time-dependent deformation of shale gas reservoir rocks and its long-term effect on the in situ state of stress. International Journal of Rock Mechanics and Mining Sciences 69:120-132

Tan Y, Wang S, Rijken M, Hughes K, Ning ILC, Zhang Z, Fang Z (2021) Geomechanical Template for Distributed Acoustic Sensing Strain Patterns during Hydraulic Fracturing. SPE Journal 26:627-638

Vachaparampil A, Ghassemi A (2017) Failure characteristics of three shales under true-triaxial compression. International Journal of Rock Mechanics and Mining Sciences 100:151-159

Van Dam D, De Pater C Roughness of hydraulic fractures: The importance of in-situ stress and tip processes. In: SPE Annual Technical Conference and Exhibition, 1999. OnePetro,

Van Dam D, De Pater C, Romijn R (2000) Analysis of hydraulic fracture closure in laboratory experiments. SPE Production & Facilities 15:151-158

Vinci C, Renner J, Steeb H (2014) A hybrid-dimensional approach for an efficient numerical modeling of the hydro-mechanics of fractures. Water Resources Research 50:1616-1635

Wang H (2019) Hydraulic fracture propagation in naturally fractured reservoirs: Complex fracture or fracture networks. Journal of Natural Gas Science and Engineering 68:102911

Wang S, Sloan S, Fityus S, Griffiths D, Tang C (2013) Numerical modeling of pore pressure influence on fracture evolution in brittle heterogeneous rocks. Rock mechanics and rock engineering 46:1165-1182

Weinberg RF, Regenauer-Lieb K (2010) Ductile fractures and magma migration from source. Geology 38:363-366

Wong T-f, Baud P (2012) The brittle-ductile transition in porous rock: A review. Journal of Structural Geology 44:25-53

Wrobel M, Papanastasiou P, Dutko M (2022) On the pressure decline analysis for hydraulic fractures in elasto-plastic materials. arXiv preprint arXiv:220206581

Wu R (2006) Some fundamental mechanisms of hydraulic fracturing. Georgia Institute of Technology,

Yang Y, Liu S, Chang X (2021) Fracture stiffness evaluation with waterless cryogenic treatment and its implication in fluid flowability of treated coals. International Journal of Rock Mechanics and Mining Sciences 142:104727

Yu B, Liu C, Chen W, Lu J, Liu Y (2022) Experimental study on deformation and fracture characteristics of coal under different true triaxial hydraulic fracture schemes. Journal of Petroleum Science and Engineering 216:110839

Zeng L, Reid N, Lu Y, Hossain MM, Saeedi A, Xie Q (2020) Effect of the fluid–shale interaction on salinity: implications for high-salinity flowback water during hydraulic fracturing in shales. Energy & Fuels 34:3031-3040

Zhang J, Davis DM, Wong T-F (1993) The brittle-ductile transition in porous sedimentary rocks: Geological implications for accretionary wedge aseismicity. Journal of Structural Geology 15:819-830

Zhang X, Jeffrey RG, Thiercelin M (2009) Mechanics of fluid-driven fracture growth in naturally fractured reservoirs with simple network geometries. Journal of Geophysical Research: Solid Earth 114

Zhang Z et al. (2020) Modeling of fiber-optic strain responses to hydraulic fracturing. Geophysics 85:A45-A50

Zhou J, Chen M, Jin Y, Zhang G-q (2008) Analysis of fracture propagation behavior and fracture geometry using a tri-axial fracturing system in naturally fractured reservoirs. International Journal of Rock Mechanics and Mining Sciences 45:1143-1152

Zoback, M. D., & Kohli, A. H. (2019). *Unconventional reservoir geomechanics*. Cambridge University Press.